

# Principles and Metrics of Extreme Learning Machines Using a Highly Nonlinear Fiber

Mathilde Hary,<sup>1,2, a)</sup> Daniel Brunner,<sup>2</sup> Lev Leybov,<sup>1</sup> Piotr Ryzkowski,<sup>1</sup> John M. Dudley,<sup>2</sup> and Goëry Genty<sup>1</sup>

<sup>1)</sup> Photonics Laboratory, Tampere University, FI-33104 Tampere, Finland

<sup>2)</sup> Université Marie et Louis Pasteur, CNRS UMR 6174, institut FEMTO-ST, 25000, Besançon, France

(Dated: 10 January 2025)

Optical computing offers potential for ultra high-speed and low latency computation by leveraging the intrinsic properties of light. Here, we explore the use of highly nonlinear optical fibers (HNLFs) as platforms for optical computing based on the concept of Extreme Learning Machines. Task-independent evaluations are introduced to the field for the first time and focus on the fundamental metrics of effective dimensionality and consistency, which we experimentally characterize for different nonlinear and dispersive conditions. We show that input power and fiber characteristics significantly influence the dimensionality of the computational system, with longer fibers and higher dispersion producing up to 100 principal components (PCs) at input power levels of 30 mW, where the PC correspond to the linearly independent dimensions of the system. The spectral distribution of the PC's eigenvectors reveals that the high-dimensional dynamics facilitating computing through dimensionality expansion are located within 40 nm of the pump wavelength at 1560 nm, providing general insight for computing with nonlinear Schrödinger equation systems. Task-dependent results demonstrate the effectiveness of HNLFs in classifying MNIST dataset images. Using input data compression through PC analysis, we inject MNIST images of various input dimensionality into the system and study the impact of input power upon classification accuracy. At optimized power levels we achieve a classification test accuracy of 88%, significantly surpassing the baseline of 83.7% from linear systems. Noteworthy, we find that best performance is not obtained at maximal input power, i.e. maximal system dimensionality, but at more than one order of magnitude lower. The same is confirmed regarding the MNIST image's compression, where accuracy is substantially improved when strongly compressing the image to less than 50 PCs.

## I. INTRODUCTION

Optical computing has emerged as a promising model for addressing the growing demands of high-speed and energy-efficient computation<sup>1</sup>. By leveraging the unique properties of light, such as high bandwidth and parallelism, optical systems offer significant advantages over traditional electronic architectures. This is particularly true for tasks involving real-time computing of ultrafast phenomena and ultrafast metrology<sup>2</sup>. For such applications, electronics impose a GHz bandwidth limitation which is elegantly mitigated using photonics. Computing approaches inspired by neural networks require a large number of linear connections and nonlinear transformations that preserve the time scale of the input data sample. The nonlinear dynamics of photonic systems, and in particular those associated with the propagation of light in optical fiber therefore have the potential to significantly expand the horizon of real-time computing into the femtosecond (fs) domain. However, fully implementing practical and programmable, i.e. trainable optical computing platforms for such tasks in hardware remains to be demonstrated.

Artificial Neural Networks (ANNs) have become a cornerstone of modern computation due to their ability to process high-dimensional data effectively. The inherent

parallelism of light has the potential to accelerate computations to unprecedented speeds. The fundamental physics of optical signal transduction allows preserving the input-data timescales up to THz bandwidths, which is fundamentally out of range for electronics which usually are limited to GHz input data bandwidths. However, mapping such concepts, in particular traditional ANNs and deep ANN architectures onto physical hardware induces significant challenges. These challenges are especially pronounced in optical systems, where iterative training methods such as backpropagation are difficult to implement in hardware<sup>3</sup>, which leads to either using computationally expensive physical-twin optimization<sup>4</sup> or gradient-free methods<sup>5-7</sup>.

To significantly mitigate these challenges, single-layer feed-forward networks such as Extreme Learning Machines (ELMs)<sup>8</sup> have been proposed as a hardware-friendly alternative<sup>9</sup>. Extreme Learning Machines bypass the need for iterative weight optimization by maintaining the often randomly initialized input weights and biases fixed during training, while output weights can be computed in a single step using linear regression<sup>10</sup>. Conceptually speaking, ELMs transform input data into a high-dimensional representation by random nonlinear mappings, where many problems become linearly separable, simplifying computation without compromising accuracy. This approach dramatically reduces the complexity of training while leveraging the intrinsic speed of optical hardware<sup>9</sup>.

Optical systems, including electro-optical<sup>9</sup>,

<sup>a)</sup> Electronic mail: [mathilde.hary@tuni.fi](mailto:mathilde.hary@tuni.fi)

nanophotonics<sup>11</sup>, metasurfaces<sup>12</sup>, and silicon photonics<sup>13</sup>, have shown particular promise as platforms for implementing ELMs. The high-speed nature of optical signal transduction enables implementing an ANN's connections without the usual limitations by an RC-time constant of an electronic circuit. These connections are a key component of neural networks, and optics allows them to be efficiently performed in parallel, in some cases enabling computation at the speed of light.

It is important to emphasize that not only is linear mixing essential but that also nonlinear operations must be carried out in real-time and at ultrafast speed. In this context, the nonlinear propagation of short pulses in optical fibers arising from the instantaneous Kerr effect can potentially fulfill this requirements. Recently, fiber optics systems have indeed been successfully exploited for pattern decoding and image classification<sup>14</sup>.

Here, we investigate experimentally the potential of single-mode nonlinear fibers as a computational platform for future ultrafast timescale input data. The fs input pulses used for seeding the optical ELM demonstrate that real-time phenomena on these timescales can be injected and processed by the system. The ONN-topology is a hybrid between a reservoir computer<sup>15</sup> and an ELM<sup>8</sup>, and we encode information by modulating the spectral phase of short pulses injected into a highly nonlinear fiber. The ELM's internal layer state corresponds to the nonlinearly broadened optical spectrum at the fiber output, and the readout weights are digitally multiplied onto the spectrum to create the system's output in an offline procedure<sup>10</sup>. The ELM's nonlinearity is provided by the instantaneous optical Kerr effect, which can be described by the generalized nonlinear Schrödinger equation (NLSE). Propagation induces continuous evolution of the nonlinear transformation, yet consecutive input-states are disjoint due to the pulsed optical injection. As such, nonlinear mixing in the system is akin to an RC, yet the system does not exhibit working memory, which is akin to an ELM or a reservoir in its steady state. Our study focuses on understanding how fiber properties, such as dispersion, length, and nonlinearity affect the system's computational capacity, which we gauge through task-independent evaluations<sup>16</sup>. We experimentally characterize a physical ANN's principle computing metrics, effective dimensionality as well as consistency, as a function of input power for numerous fibers with different dispersion and nonlinear characteristics, as well as the dimensionality of injected data for the first time in an NLSE system. Finally, we assess the system's performance in classification tasks using the MNIST handwritten digit dataset for numerous combinations of input dimensionality and input power, also comparing the performance of an HNLF and a standard single-mode fiber.

## II. CONCEPTS AND OPTICAL COMPUTING HARDWARE

### A. The structure of an Extreme Learning Machine

Reservoir computers and ELMs provide an efficient approach to ANN training by eliminating the iterative optimization of hidden layer parameters. As our HNLF optical computer lacks the ability of transient computing with the associated short-term memory, we will refer to our systems as an ELM. The network's architecture consists of an input layer comprising  $d$  dimensions (neurons or features), a single hidden layer with  $l$  dimensions, and an output layer with  $k$  dimensions, see Fig. (a). Considering input data with  $N$  samples, the input data matrix  $\mathbf{X} \in \mathbb{R}^{N \times d}$  represents the complete input data set. The distinguishing feature of ELMs lies in input weights and hidden layer biases remaining fixed throughout the training process. Often they are even initialized randomly, yet in a hardware implementation, they are usually determined by the physics inherent to data injection as well as the nonlinear system's properties. The hidden layer performs a nonlinear transformation of the input data, and mathematically this transformation is of the type

$$\mathbf{H} = g(\mathbf{X}\mathbf{W}^{\text{in}} + \mathbf{b}), \quad (1)$$

where  $\mathbf{H}$  is the ELM's hidden layer state for all  $N$  input samples,  $\mathbf{W}^{\text{in}} \in \mathbb{R}^{d \times l}$  is a fixed and often randomly initialized matrix connecting input and hidden layer,  $\mathbf{b} \in \mathbb{R}^l$  is the hidden layer bias vector, and  $g(\cdot)$  is the ELM's nonlinear activation function. Common choices for  $g(\cdot)$  in software ELMs include the sigmoid, ReLU, or hyperbolic tangent functions, and nonlinearity is required in order to enhance the feature representation of the injected data. In our experiment,  $g$  is implemented through nonlinear propagation in the fiber, and  $\mathbf{H}$  is the spectrum at the fiber's output.

The ELM's output  $\mathbf{Y}$  containing  $m$  features or neurons is computed for all  $N$  input samples contained in  $\mathbf{X}$  by linearly combining the hidden layer states according to

$$\mathbf{Y} = \mathbf{H}\mathbf{W}^{\text{out}}, \quad (2)$$

where  $\mathbf{W}^{\text{out}} \in \mathbb{R}^{l \times m}$  is the output weight matrix connecting the hidden layer to the output layer. In our experiment,  $\mathbf{H}$  is determined with an optical spectrum analyzer (OSA), and weights  $\mathbf{W}^{\text{out}}$  are digitally applied in a post-processing step. Training the ELM involves determining  $\mathbf{W}^{\text{out}}$  such that the predicted outputs  $\mathbf{Y}$  closely match the target outputs  $\mathbf{T} \in \mathbb{R}^{N \times m}$ . The objective is typically formulated as the minimization of a loss function, which often is the mean squared error between  $\mathbf{Y}$  and  $\mathbf{T}$ :

$$\text{Loss} = \|\mathbf{H}\mathbf{W}^{\text{out}} - \mathbf{T}\|^2. \quad (3)$$

To solve for  $\mathbf{W}^{\text{out}}$ , ELMs leverage a closed-form solution through least-squares regression:

$$\mathbf{W}^{\text{out}} = \mathbf{H}^\dagger \mathbf{T}, \quad (4)$$

where  $\mathbf{H}^\dagger$  is the Moore-Penrose pseudoinverse of  $\mathbf{H}$ . In order to avoid overfitting one often uses Ridge regression instead of Eq. 4, however, when implementing the ELM in physical systems the ELM’s internal as well as data-injection noise effectively regularizes  $\mathbf{W}^{\text{out}}$  and overfitting is rarely a problem<sup>10</sup>.

This particular training concept has several key benefits for proof-of-concept implementations in hardware as well as for full hardware implementations including in-situ learning<sup>5,6</sup>. It bypasses the need for backpropagation and iterative optimization. Firstly, this enables rapid training by obtaining a final  $\mathbf{W}^{\text{out}}$  in a single shot through standard numerical approximation methods like the *pinv* function of Matlab. Secondly, training does not modify any parameters but the readout weights, hence one can inject all  $N$  input samples in one sequence and utilize a single recording of  $\mathbf{H}$  for the entire training step. This would be impossible beyond ELM and RC architectures, where training inherently alters  $\mathbf{H}$ , which hence has to be re-determined has to be repeated after each weight update.

## B. Experimental implementation

The experimental setup used in this study builds upon a previously reported configuration<sup>17</sup>. The setup features a 4-f line with a spatial light modulator (SLM, Holoeye Pluto 2.1) positioned in the Fourier plane in a folded arrangement. The pump laser (NKT Photonics ORIGAMI) delivers pulses with a duration of 235 fs at a repetition rate of 40.9 MHz, a FWHM bandwidth of 14 nm, and a beam diameter of 5 mm before entering the fiber via a focusing lens (Thorlabs AC-254-030-CM-L). For an input power of 39 mW, the generated spectral broadening spans from 1200 nm to 2200 nm when no phase pattern is applied. However, here the focus is on the 1500-2200 nm band to align with the measurement range of the optical spectrum analyzer (OSA, Yokogawa AQ6376). The SLM is used to update the phase pattern of the input light, which is horizontally spread over 1000 SLM pixels, corresponding to the spread of the Gaussian pulse on the Spatial Light Modulator (SLM), and repeated vertically 1080 times to match the height of the SLM. The SLM modulates the input optical beam, which propagates through the HNLF, producing spectral responses sampled across  $l = 3000$  points spanning the wavelength range of 1500 to 2200 nm. In order to study the impact of nonlinear propagation based on different dispersion parameters we studied certain aspects of the photonic ELM for a variety of fibers. Each fiber was 5 meters long with 20 cm of standard single-mode fiber (SMF28) patch cords spliced onto both ends, and Fig. 1(c) shows typical output spectra on a logarithmic as well as on a linear and normalized scale.

The maximal optical collection efficiency of the injected pulse was approximately 55 %. This was primarily limited by splice-losses as well the coupling efficiency from free-space propagation into the first SMF28 fiber.

However, the spectral phase applied via the SLM results in diffraction, while injection into the SMF28 creates spatial filtering through the fiber’s mode profile. This can make the coupling efficiency sensitive to the input dimensionality  $d$  and the particular phase pattern  $\mathbf{X}$ . We systematically evaluate these effects in Section III A. For each of the following evaluations, we used Fiber 1 with anomalous dispersions, apart from the section where we focus specifically on the impact of dispersion, where we compare all three fibers.

## C. Principal Component Analysis

Principal Component Analysis (PCA) is a statistical technique widely used for dimensionality reduction, feature extraction, and data visualization. By transforming the original data into a new set of uncorrelated variables, known as principal components (PCs), PCA captures the directions of maximum variance within a dataset. This identifies dominant patterns and allows mitigating redundancies while preserving as much relevant information as intended by keeping dominant PCs and discarding those below an ad-hoc defined relevance threshold.

To formally define PCA, let  $\mathbf{X} \in \mathbb{R}^{N \times f}$  represent a dataset consisting of  $N$  samples, each described by  $f$  features. In this representation, each of the  $N$  rows of  $\mathbf{X}$  corresponds to a data sample, and each of the  $f$  columns represents a feature. The goal of PCA is to project data  $\mathbf{X}$  onto a set of orthogonal axes such that the variance along each axis is maximized. These axes are the PCs, and they are linear combinations of the original features  $f$ .

The PCA process begins with data centering, where the mean of each feature is subtracted to ensure that the dataset has a mean of zero, which is crucial for correctly computing the covariance. The centered dataset  $\mathbf{X}^c$  is calculated as

$$\mathbf{X}^c = \mathbf{X} - \mathbf{1}\mu^{(T)}, \quad (5)$$

where  $\mathbf{1}$  is a  $N \times 1$  column vector of ones,  $\mu \in \mathbb{R}^f$  is the vector of feature means and  $(T)$  is the transpose of a vector or matrix. Next, the covariance matrix  $\mathbf{C} \in \mathbb{R}^{f \times f}$  is computed to capture the relationships between features by

$$\mathbf{C} = \frac{1}{N-1} \mathbf{X}^{c(T)} \mathbf{X}^c. \quad (6)$$

$\mathbf{C}$  encapsulates the variance of each feature along its diagonal and the pairwise covariances between features in its off-diagonal elements. The PCs are then derived from the eigenvalues and eigenvectors of the covariance matrix. Let  $\mathbf{\Lambda} \in \mathbb{R}^{f \times f}$  be the diagonal matrix of eigenvalues and  $\mathbf{V} \in \mathbb{R}^{f \times f}$  be the matrix of corresponding eigenvectors, such that

$$\mathbf{C}\mathbf{V} = \mathbf{V}\mathbf{\Lambda}. \quad (7)$$

The columns of  $\mathbf{V}$  are eigenvectors providing the directions of maximum variance in the dataset, while the associated eigenvalues in  $\mathbf{\Lambda}$  quantify the variance along each

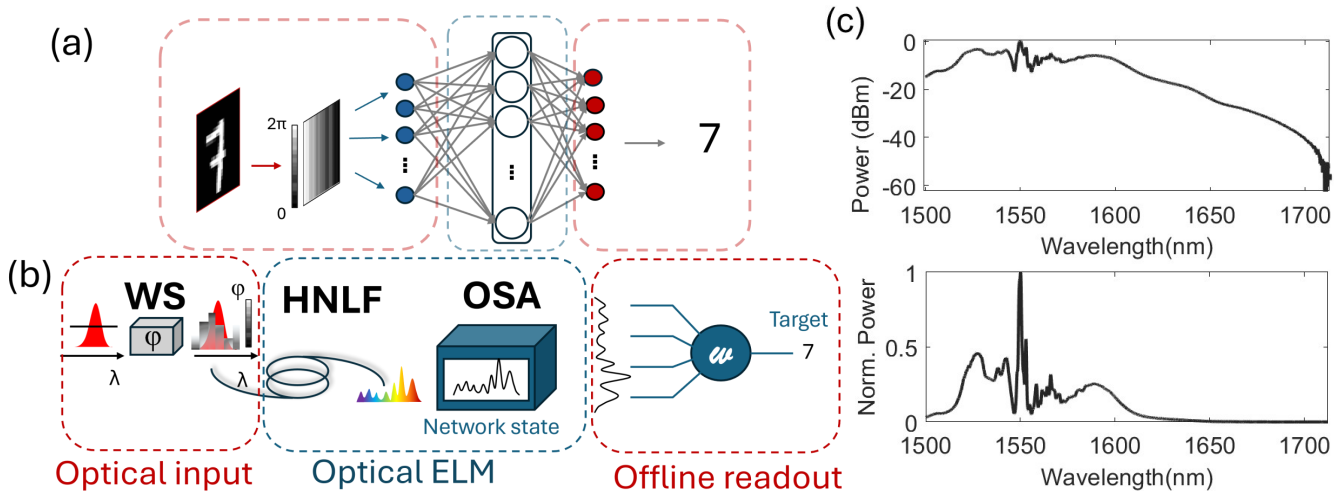


FIG. 1. (a) conceptual diagram of the ELM (b) schematic of the experimental setup for the Extreme Learning Machine implementation composed of a waveshaper (WS), highly nonlinear fiber (HNLf), and Optical spectrum analyzer (OSA) to collect the output fiber spectra. Typical encoding patterns are depicted for both cases of task dependant and task independent. (c) typical fiber output spectra in logarithmic and linear scale for an input dimension  $d = 20$  and an input power  $P_{in} = 35$  mW.

of these PCs. Sorting the diagonal entries in  $\mathbf{\Lambda}$  in descending magnitude sorts the eigenvalues according to their relevance for the linear reconstruction of the original data  $\mathbf{X}$ . By selecting the top  $k$  eigenvectors associated with the largest eigenvalues enables dimensionality reduction while preserving the most significant patterns in data  $\mathbf{X}$ .

The reduced dataset, denoted as  $\mathbf{X}^{\text{PCA}}$ , is obtained by projecting the centered data onto the subspace spanned by the selected eigenvectors according to

$$\mathbf{X}^{\text{PCA}} = \mathbf{X}^c \mathbf{V}^{\text{PCA}}, \quad (8)$$

where  $\mathbf{V}^{\text{PCA}} \in \mathbb{R}^{f \times k}$  contains the top  $k$  eigenvectors. This transformation reduces the dimensionality of the data from  $f$  to  $k$ .

We employ PCA in two different settings; (i) during our task-independent analysis we use PCA in order to determine the effective dimensionality of the optical ELM, while (ii) for the task-dependent analysis we leverage PCA to study the computational accuracy of our ELM as a function of input parameters. Setting (i), leveraging PCA as for dimensionality study, is an essential concept to physical, non-conventional computing systems, see explanation in Section III A. For setting (ii) we leverage the linear data compression aspect of PCA in order to evaluate our hardware ELM's capacity to expand the number of features  $d$  in the input data onto ELM space dimensionality  $l$ . In that context, we compress the dimensionality of input data to  $d$  via PCA and analyze the dimensionality of the ELM's response using PCA, see explanation in Section III B.

### III. RESULTS

In the following, we investigate the ELM's performance using various metrics. Three different HNLf's are used at various stages of our experiments, and their dispersion characteristics, measured over the range of 1500 to 1620 nm, are shown in Fig. 3(a). At the pump wavelength  $\lambda_{\text{pump}} = 1559.4$  nm, the dispersion coefficients are

- $D_{\text{fiber 1}} = -0.98$  ps/(nm·km) (normal dispersion, relatively flat phase profile).
- $D_{\text{fiber 2}} = 0.046$  ps/(nm·km) (near zero-dispersion: anomalous dispersion above  $\lambda_{\text{pump}}$  and normal dispersion below).
- $D_{\text{fiber 3}} = 0.33$  ps/(nm·km).

We used Fiber 1 with normal dispersion across the entire spectrum for each of the following evaluations, while for in the section where we focus specifically on the impact of dispersion, where we compare all three fibers.

#### A. Task-Independent performance metrics

In the context of ANN computing, the number of non-linear (hidden) layers as well as the neurons within are one of the determining features. Final computing performance sensitively depends on these, and as such both numbers are what determines the overall architecture of vanilla ANNs. Yet, in the context of unconventional computing substrates, one can face a dilemma when attempting to specify the number of hidden layer neurons, here  $l$ . The number of hidden layer neurons  $l$  is clearly defined when implementing an ELM in a classical software/code

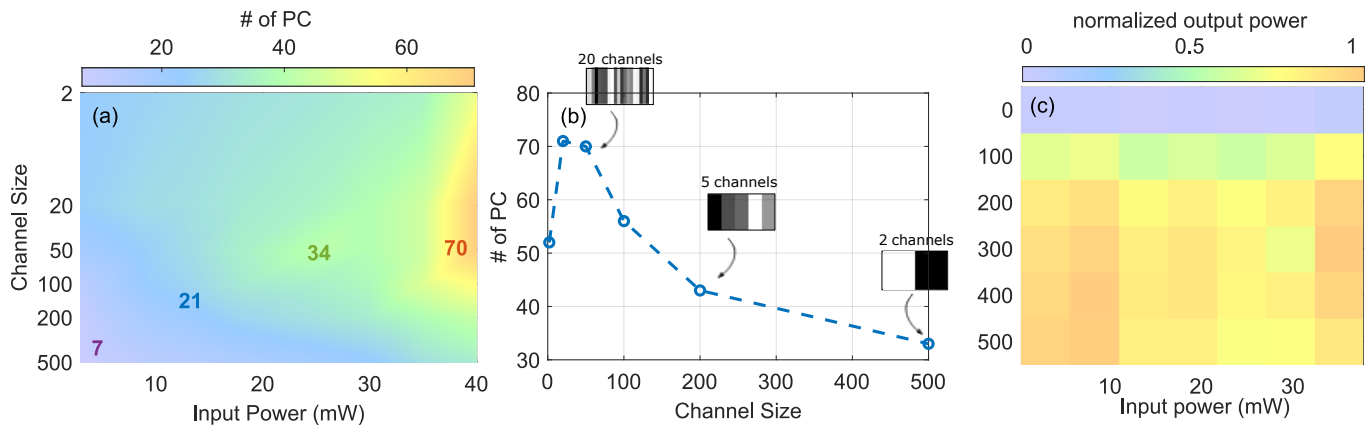


FIG. 2. (a) Principal Component Analysis (PCA) results showing the effect of varying input power and channel size on the number of principal components (PCs). The color gradient indicates the number of PCs, with warmer colors representing fewer PCs and cooler colors representing a higher number of PCs. This highlights the regions of channel size and input power combinations that maximize or minimize the complexity of the system response. (b) Number of PCs as a function of channel size for a fixed input power of 40 mW, illustrating the trend and identifying the optimal channel size for this input power level. The insets display example Spatial Light Modulator (SLM) patterns and their respective number of channels for selected channel sizes (50, 200, and 500), providing a visual representation of the corresponding SLM configuration at these sizes. (c) Integral over power spectral density measured by the OSA, normalized by the injected power. Optical losses are essentially independent of the injected power.

setting or in a hardware comprising discrete units acting as its neurons. However, when encoding ELM state  $\mathbf{H}$  in a continuous physical dimension, then this dimensionality is obscured within the continuous spectrum of values<sup>16</sup>, here the power spectral density of the broadened optical output spectrum obtained by the OSA. The general approach for assessing the spectrum's number of features, i.e. neurons, is to finely discretize this spectrum via high-resolution sampling and then linearly project this spectrum onto a set of orthogonal dimensions sorted by relevance. One method is using a set of orthogonal functions as projection space<sup>18</sup>, here we employ PCA. In the context of our optical ELM implementation, such analysis corresponds to obtaining the dimensionality encoded within output spectra that can be leveraged for computing. An fs input pulse covering 14 nm and whose spectral phase was modulated by the input information can readily be broadened to a large spectrum covering several hundred nm by its nonlinear propagation. However, if this spectrum itself is (partially) comprised of broad spectral features, and these features react highly similarly to changes in the input information, then the dimensionality of the underlying ELM in the context of computing is low, i.e. an ELM with few neurons. In other words, it is not the spectral width of a spectrum but the number of linearly independent spectral features controllable within that determines a spectral broadening's value for computing.

For determining our ELM effective dimensionality we use the introduced PCA analysis and modulate the input pulse's spectral phase with random patterns. For this experiment,  $N = 3000$  random patterns were generated, each comprising  $d$  random values uniformly dis-

tributed between 0 and  $2\pi$ . Following nonlinear propagation, spectra were concatenated to form matrix  $\mathbf{H}$ , on which PCA was performed. Eigenvalues and eigenvectors were computed and sorted, with the cumulative sum of eigenvalues used to determine the number of PCs required to retain 95 % of the variance. This threshold was taken as the measure of computational dimensionality provided by the HNLF ELM implementation, which we refer to as  $PC^{95}$ . Furthermore, we used matrix  $\mathbf{H}$  to evaluate the system's consistency, which gauges a systems capacity to act as a reliable computer.

### ELM dimensionality and physical input channel size

First on the list of our general HNLF ELM characterization is the impact of the physical size of each input channel. Channel sizes explored include 2, 20, 50, 100, 200, and 500 SLM pixels, which for the 10,000 illuminated pixels results in  $d \in \{500, 100, 50, 25, 15, 5, 2\}$ , respectively. The pitch between SLM pixels is  $8 \mu\text{m}$ , and 14 nm input pulse spectrum covers  $\sim 1100$  pixels, resulting in  $\sim 0.013$  nm/pixel. The results, presented in Fig. 2, reveal the strong impact of input channel size and hence  $d$  on the ELM's effective dimensionality  $PC^{95}$  under varying input power levels. Overall, the dimensionality of the system increases with input power for all channel configurations. Figure 2(b) focuses on a fixed input power of  $P_{\text{in}} = 40$  mW, for which we obtain a maximum value of  $PC^{95} = 70$  for channel sizes between 20 and 50 pixels. Insets in Fig. 2(b) illustrate typical SLM patterns corresponding to selected channel sizes (50, 200, and 500), providing a visual representation of the input configu-

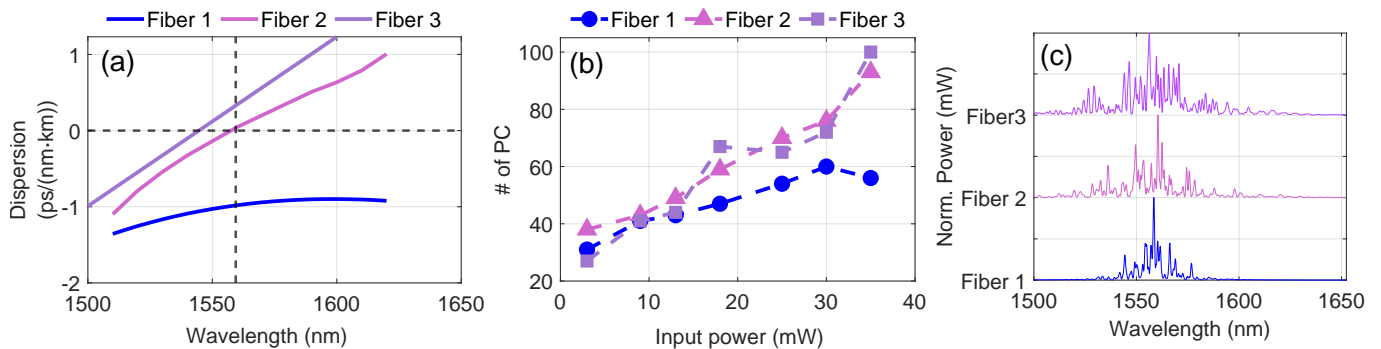


FIG. 3. (a) Dispersion as a function of wavelength for three fibers (Fiber 1, Fiber 2, and Fiber 3). Fiber 1 exhibits normal dispersion with a relatively flat profile, while Fibers 2 and 3 demonstrate anomalous dispersion above the pump wavelength. (b) Number of principal components (PCs) versus input power for the three fibers. At low power, the number of PCs is similar across all fibers, and at higher power levels, Fibers 2 and 3 generate more PCs, indicating increased spectral complexity due to higher dispersion. (c) Three example spectra for the highest injection power and the three different fibers, revealing the systematic difference in spectral complexity and broadening between the normal (fiber 1) and anomalous (fibers 2 and 3) dispersion.

ration. These results suggest that intermediate channel sizes strike a balance between maintaining sufficient spatial resolution and preserving the diversity of spectral features, thus maximizing the computational capacity of the system.

Besides the effectivity of the underlying nonlinear dynamics for creating relevant ELM dimensionality, one also needs to consider the potential influence of linear effects. In Fig. 2(c) we show the integrated optical power spectral density (PSD) measured after propagation through the optical fibers and normalized by the input power. Spectral phase modulations with a spatial period smaller than 20 SLM pixels result in a noticeable drop of optical power at the fiber output. Furthermore, we examined this effect for a wide range of input powers, which reveals no systematic impact. This rules out nonlinear dynamic effects during propagation in the HNLF as underlying cause. We therefore associated this drop of output power exclusively with a loss of input coupling efficiency. The application of spatial phase modulation of the input beam by the wave-shaper results in the broadening of the focused image in the wave-shaper’s Fourier plane, where the pulse is injected into the SMF28 fiber. For a phase modulation with a sufficiently high spatial frequency, the input field at the fiber facet will increasingly deviate from an LP<sub>01</sub> mode, and coupling efficiency will therefore drop as a consequence, which is what can be seen in Fig. 2(c).

### ELM dimensionality and fiber dispersion

Dispersion is one of the main influences determining the characteristics of propagation in NLSE systems, and such such of major relevance in our context<sup>19</sup>. The spectral characteristics of spectral broadening depend sensitively on the dispersion properties of the fiber used and the associated laser pump wavelength, as these deter-

mine the details of the underlying propagation dynamics. Specifically, when an spectral broadening is seeded in the normal dispersion regime using femtosecond-picosecond pulses, the spectral broadening is typically dominated by self-phase modulation and yields smoothly varying spectral features. In contrast, seeding in the anomalous dispersion regime leads to more complex dynamics such as soliton fission, dispersive wave generation, and the Raman self-frequency shift, generally resulting in significantly more fine structure on the output spectra as well as broader spectral widths (at the same input pulse energy). These differences and the following spectral-feature widths as well as their linear correlation can hence have a significant influence on the system’s number of effective dimensionality for computing. We have examined the influence of the fiber dispersion properties on the number of PCs for three different fibers with normal, near-zero, and anomalous dispersion at the pump wavelength with dispersion curves as shown in Fig. 3(a).

For this test, we used  $d = 50$  input dimensions. The influence of fiber dispersion on the number of PCs was evaluated for the three distinct fibers introduced in Section II B exhibiting normal, near-zero, and anomalous dispersion regimes. The number of effective PCs was computed for input powers  $P_{in} \in \{3, 9, 13, 18, 25, 30, 35\}$  mW, with the results shown in Fig. 3(b). At low power levels ( $P_{in} \leq 13$  mW), the number of PCs remained relatively consistent across all fibers. However, at higher powers, the low and normal dispersion Fiber 1 produced significantly fewer PCs compared to Fibers 2 and 3. The maximum number of PCs for Fiber 1 was  $\sim 60$  at  $P_{in} = 30$  mW, while Fibers 2 and 3 with anomalous dispersion regime dynamics exhibited approximately  $PC^{95} \approx 100$  at the same  $P_{in}$  value. This suggests that the more complex spectral broadening mechanisms associated with soliton dynamics lead to output spectra on which more linearly separable features can be encoded. We attribute this physically to the lower degree of

internal correlation across a broadband spectrum when compared to spectra generated from the normal dispersion dynamics of self-phase modulation. The systematic differences between the normal (fiber 1) and anomalous (fibers 2 and 3) propagation on broadening and number of spectral features around the seeding wavelength can be seen in Fig. 3(c). Furthermore, the number of features around the pump for fiber 1 is smaller than for fibers 1 and 2, explaining the difference in  $PC^{95}$  and providing a first indicative confirmation of the earlier presented argument regarding the impact of dispersion.

### Spectral location of computing dimensions

One of the striking features of nonlinear fiber propagation according to the NLSE is their capacity to transform an originally  $\sim 14$  nm broad input pulse into spanning several hundred nanometers. Encode some 40 input features on these 14 nm spectral input bandwidth corresponding to  $\sim 2.6$  features/nm. Extrapolating this to the output spectrum spanning several hundreds of nanometers would result in the order a thousand features, yet as shown in the previous section this is not the case. This raises the question of where these spectrum's degrees of freedom are located, i.e. which part of the spectral broadening does contribute significantly to the  $PC^{95}$ . Since PCA is a linear technique based on projecting the original features, here the sampling positions of the optical spectra, onto the orthogonal space of PCs via  $\mathbf{V}$ , one can use this matrix to show how individual PC eigenvectors are associated to spectral positions. Fig. 4(a) show this spectral loading for the first three principal components for  $P_{in} = 35$  mW and  $d = 50$  input samples, combined with the original optical output spectrum on a linear scale. One can clearly see that the wavelengths involved in creating the  $PC^{95}$  are located very closely around the input pulse, roughly within a width of  $\pm 40$  nm.

This has two main reasons, which are linked to the particularities of computing. Firstly, the PSD of spectral broadening dynamics spanning hundreds of nanometers is clearly discernible on the usually employed logarithmic scales of dBm. However, a computer's output relies at some stage on combining these different spectral intensities according to some ratio. In order to leverage the different features encoded in wavelengths, one needs to be able to balance these different features to create a desired output. In other words, if one wants to leverage spectral components of a spectral broadening that have a 60 dB difference in their power, one has the choice of either attenuating the higher PSD feature to the level of the lower before applying the relative scaling, hence substantially sacrificing efficiency and signal to noise ratio. Or one has to rely on  $\log_2(1/[10^{-6}/256]) \sim 28$  bit resolution weights to achieve only 8-bit resolution in  $\mathbf{W}^{out}$ , making a hardware implementation of the readout realistically impossible and as a consequence most likely also a realtime implementation.

Secondly, a simple visual analysis of typical spectra shows that around the pump wavelength, different spectral features are quite narrow, of the order 1 nm, while these widths change to 10s of nm in the regions of the spectral broadening further away from the pump. Linearly independent dynamics creating independent PCs can only be provided by spectral components that too are linearly uncorrelated as a response to input modulations, and the lower limit of spectral density of such uncorrelated components is determined by their spectral widths, similar to the Rayleigh criterion in imaging. Broadband soliton dynamics for example, mainly responsible for spectral broadening, can therefore only contribute in a limited capacity to an optical ELM's computational dimensionality  $PC^{95}$ . We have measured these loadings for a wave-shaper including as well as excluding the 0<sup>th</sup> diffractive order in the injected signal, and no systematic difference was found. Heuristically speaking this is reasonable; compared to 1<sup>st</sup> order only spectral broadening seeding, including the 0<sup>th</sup> order creates an interference between the fully phase-modulated 1<sup>st</sup> order and the unmodulated part of the 0<sup>th</sup> order. Interference corresponds to the superposition of the two optical fields, and in a physics context the superposition principle is inherently linear, hence does not augment the feature dimensionality, yet it could potentially be interpreted as influencing injection weights  $\mathbf{W}^{in}$ . For 1<sup>st</sup> order only spectral broadening seeding we added a constant blazed grating to the phase profile of the SLM and only collected the 1<sup>st</sup> diffracted order, which was achieved by adding a saw-tooth pattern to  $\mathbf{X}$ .

### ELM dimensionality and fiber length

We investigated the impact of fiber length as another critical parameter influencing spectral broadening and hence potential computational capacity. The experiment was repeated for Fiber 1 at lengths of 1, 2, and 5 meters. The number of PCs as a function of input power is shown in Fig. 4(b). The results reveal a clear dependence on fiber length. The 5-meter fiber consistently produced a higher number of PCs compared to the shorter fibers at equivalent input powers. For instance,  $PC^{95}$  increased from approximately 30 to 60 for the 5-meter fiber as  $P_{in}$  increased from 3 to 35 mW. In comparison, the 1-meter fiber exhibited a slower increase, with  $PC^{95}$  rising from approximately 30 to 40 over the same power range. These findings suggest that longer fibers enhance the dimensionality of the output spectra.

### Consistency of the ELM

The dimensionality described in the previous sections is however only one-half of the fundamental requirements for an ANN-based function approximator such as our physical ELM. The other half is consistency, which de-

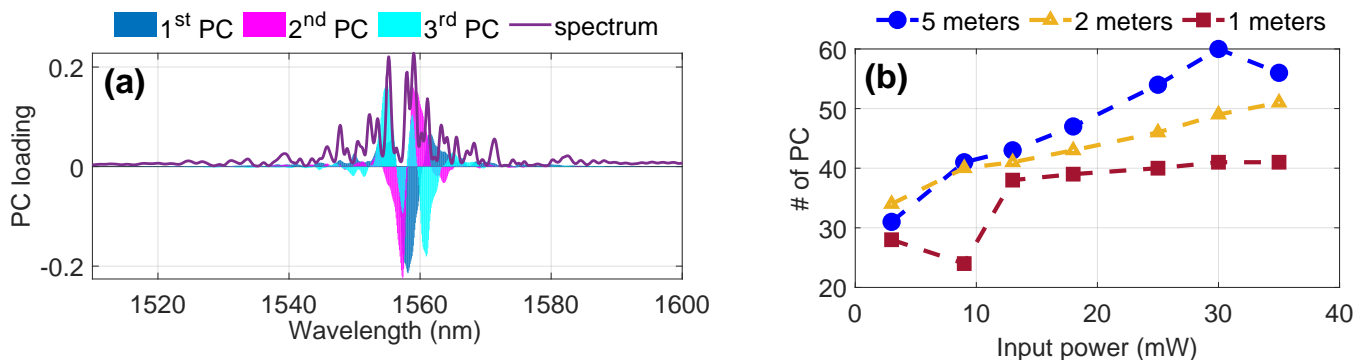


FIG. 4. (a) Spectral distribution of the PCs shows that the ELM’s feature space relies mostly on dynamics close to the pump wavelength. (b) Number of principal components (PCs) as a function of input power for three different fiber lengths (1, 2, and 5 meters). The 5-meter fiber consistently exhibits a higher number of PCs compared to shorter fibers, indicating that longer fibers enhance the dimensionality of the output spectra.

termines the capacity of such a system to respond in a reliable and reproducible manner to identical input information. A heuristic analogy can be made to a classical computer program when ignoring exotic examples of chaotic system simulations and comparable scenarios: executing the same computer code numerous times using the same user or data input generally produces the same outcome with a very high probability. The opposite, the same code leading to different outcomes, usually renders the computer or the code inept to address relevant computing tasks. In dynamical systems, the capacity to react to repeated input with similar responses is determined by a system’s consistency<sup>20,21</sup>, and inconsistency renders reproducible computing with fully chaotic systems impossible until today. For that, we constructed  $\mathbf{X}$  using  $N = 4000$  and  $d = 50$ , where the  $N$  input samples are all identical, random, and uniformly distributed phase patterns. The concatenated system’s output spectra  $\mathbf{H}$  are then used to calculate the correlation coefficient between all  $N$  responses, and the resulting correlation matrix is shown in Fig. 5(a,b) for  $P_{\text{in}} = 3$  mW and  $P_{\text{in}} = 35$  mW, respectively.

Each of the  $N$  responses in  $\mathbf{H}$  is an optical spectrum averaging numerous pulses, and as such the signal-to-noise ratio can be very high, as can be seen by the above 99.7% correlation in Fig. 5(a) that was obtained for  $P_{\text{in}} = 3$  mW. Importantly, such high correlations are also regularly achieved with real-time implementations. Two signatures are visible from these measurements. The first is the spectra-to-spectra fluctuations, and the other is the long-term drift of such a system. The impact of the first is visible as entries close to the correlation matrix’s diagonal, while the latter are located towards the top-right and bottom-left corners. The correlation matrix is symmetric to its diagonal since zero-lag correlations in non-quantum systems are symmetrical. However, when increasing the optical injection power to  $P_{\text{in}} = 35$  mW, then the general level of correlation drops substantially, with a minimum of  $\sim 62\%$ , see Fig. 5(b). Furthermore, the overall structure too is altered, now exhibiting signif-

icant drops in correlation located close to the matrix’s diagonal. The system’s stability is therefore reduced in the context of, both, spectra-to-spectra correlations as well as with regards to long-term stability.

A system’s consistency is determined by the average value to the correlation matrix’s upper triangle<sup>20</sup>, and in Fig. 5(c) we show the consistency’s dependency for a range of  $P_{\text{in}}$ . Consistency monotonously reduces for increasing  $P_{\text{in}}$  until it essentially collapses for  $P_{\text{in}} > 25$  mW. Such loss of consistency is regularly exhibited when computing with nonlinear dynamical systems<sup>22</sup>. Here, the observed drop in the correlation at higher input power could be caused by a loss of spectral coherence, a commonly observed occurrence in nonlinear spectral broadening<sup>23</sup>.

## B. Task-dependent performance metrics: MNIST Handwritten Digits Classification

### MNIST dimensionality tuning via PCA

The MNIST handwritten digit dataset was used as a benchmark task to evaluate the performance of the optical setup as a computing medium. The dataset consists of handwritten digits from 0 to 9, providing a widely used standard for classification tasks. In the previous section, we identified a non-monotonous relationship between input dimensionality  $d$  and  $\text{PC}^{95}$ , most importantly showing a decline of  $\text{PC}^{95}$  for  $d > 50$ . However, the native MNIST handwritten digits datasets comprise images of  $28 \times 28 = 784$  pixels, which, as demonstrated will reduce the dimensionality of our ELM. Most importantly, following Cover’s theorem, ELM computing leverages dimensionality expansion as a mechanism for improving computational performance as compared to simply using the input data connected to a linear layer. The input dimensionality  $d$  used for injecting the MNIST digits is therefore of major relevance. Using PCA is one possibil-



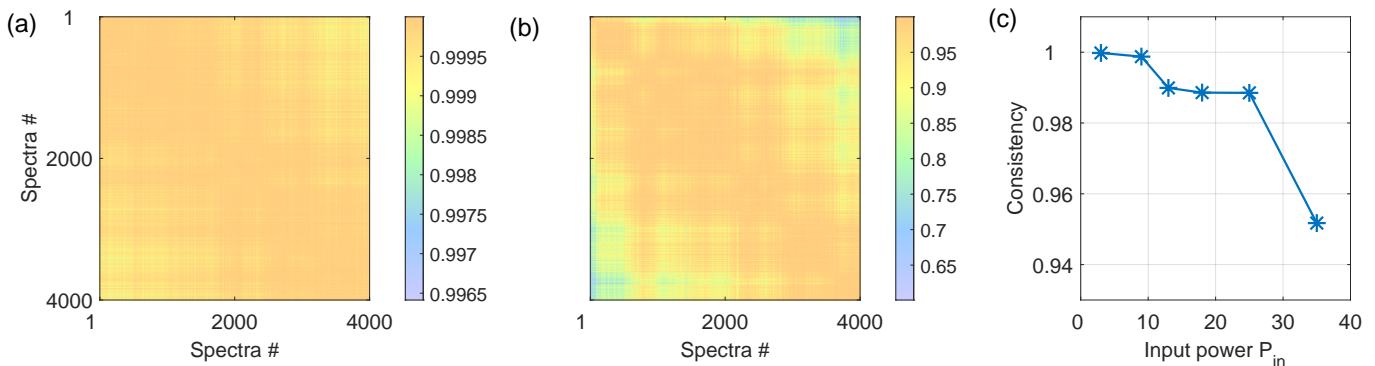


FIG. 5. Consistency of the ELM’s hidden layer state for 4000 repetitions of the same random input  $\mathbf{X}$  with  $d = 50$ . A computer’s consistent reply to identical input information is a fundamental requirement for computing. (a) and (b) show the correlation matrix between the 4000 different spectra of  $P_{in} = 3$  mW and  $P_{in} = 35$  mW, respectively. For the low injection power, the reply is close to perfectly consistent, while for  $P_{in} = 35$  mW the correlation drops down to  $\sim 0.6$  at the end of the recording. (c) Consistency, corresponding to averaging the upper triangle of the correlation matrix. Consistency monotonously decreases with  $P_{in}$ , with a significant drop for  $P_{in} > 25$  mW.

ity to adjust  $d$ , nonlinear interpolation or simple down-sampling another. However, linear down-sampling does not take the importance of certain regions into account, while nonlinear interpolation is challenging in optics to implement in hardware as it requires nonlinear spatially extended, i.e. multimode optical transformations that typically are power hungry. PCA is a linear method and hence can be implemented using linear optics<sup>24,25</sup>.

We apply PCA for image compression, as described in Section II C, to adjust the number of pixels in which we encode the MNIST images<sup>26</sup>. This reconstruction retains only the information captured by the top  $k$  PCs, with fidelity increasing as  $k$  grows; with  $k = 784$ , the reconstruction becomes exact. Figure 6(a) demonstrates the reconstruction of a sample image (‘5’) for a range of PCs. With only 5 PCs, the image is highly blurred and substantially lacks detail, by the eye it is hardly identifiable for a human. As the number of PCs increases to 20 and beyond, more features become discernible, the digit becomes progressively clearer and visible identifiable as a ‘5’. At 150 PCs, the reconstructed image closely resembles the original, with minimal information loss. These examples highlight the relationship between the number of PCs and the retention of relevant information, demonstrating that only a subset of PCs is required to preserve the essential characteristics.

Figure 6(b) and 6(c) present the classification accuracy and MSE results for training and testing datasets, using varying numbers of PCs. For that the  $d = k$  input pixels where directly connected to the  $m = 10$  outputs through a linear matrix operation  $\mathbf{Y} = \mathbf{X}^{(k)}\mathbf{W}^{out}$ , where  $\mathbf{X}^{(k)}$  is the set of  $N$  MNIST digits compressed to  $d = k$  input dimensions via PCA. Output weight matrix  $\mathbf{W}^{out}$  was computed using the Moore-Penrose pseudoinverse method as per Eq. 4, and the same weights were applied to both training and testing data. Training was done on 10,000 examples while using 1,000 examples for testing. This linear classification accuracy increases sig-

nificantly with the number of PCs, particularly between 5 and 40 PCs, where the testing accuracy improves from 0.45 to 0.83. Beyond 40 PCs, test accuracy gains start diminishing, with training accuracy continuing to rise. This plateau suggests that higher PCs primarily add redundant or noisy information, contributing little to the generalization capability of linear classifier  $\mathbf{W}^{out}$  for this size of the training data set. Similarly, the MSE decreases sharply between 5 and 40 PCs, with slower improvements thereafter. This linear classifier we set as our lower benchmark limit that our ELM needs to surpass if we want to claim the ELM actually performing relevant computing. Below this threshold, it would be computationally beneficial to compute linearly directly on the input data, which is more efficient in the general sense.

### Results with the Highly Nonlinear Fiber

For characterizing the optical ELM, the MNIST dataset was encoded with  $k = d \in \{20, 40, 784\}$  that were sent to the SLM as a phase mask. The modified optical pulse then propagated through HNLF Fiber 1. This experiment was conducted using 10,000 sample images, using a random selection of 80% of the resulting spectra for training and the remaining 20% for testing. The system’s training and classification accuracy on the test set was evaluated at various input power levels, as shown in Fig. 7. There, the red dashed line provides the linear limit for each  $k$  as explained in the previous section.

Figure 7(a) presents the results for the MNIST images with full resolution  $d = 784$ . In this configuration, the system significantly falls below the linear baseline accuracy, with accuracy consistently below 0.837 at any input power level. An optimal power level is observed around  $P_{in} = 2$  mW, achieving an accuracy of approximately 0.8. Beyond this point, no significant improve-

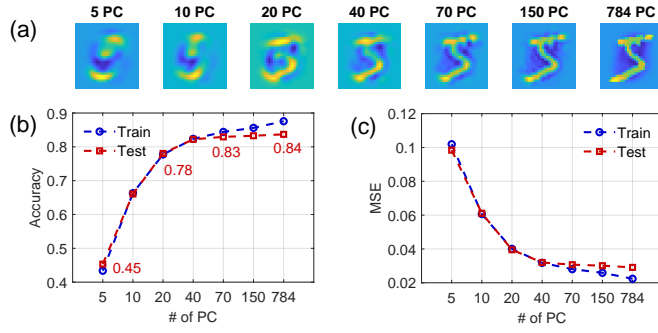


FIG. 6. (a) Reconstructing a sample MNIST image using  $k \in [5, 10, 20, 40, 70, 150, 784]$  principal components (PCs), illustrating the gradual improvement in image fidelity as more PCs are used. Training as well as testing (a) accuracy and (b) MSE for a linear classifier as a function of the number of PCs, showing improved accuracy with increased PCs. These results represent the linear benchmark that the optical ELM needs to surpass in order to claim relevant computing. Testing performance saturates for  $k > 70$  PCs. Training is done on 10000 examples while testing is done on 1000.

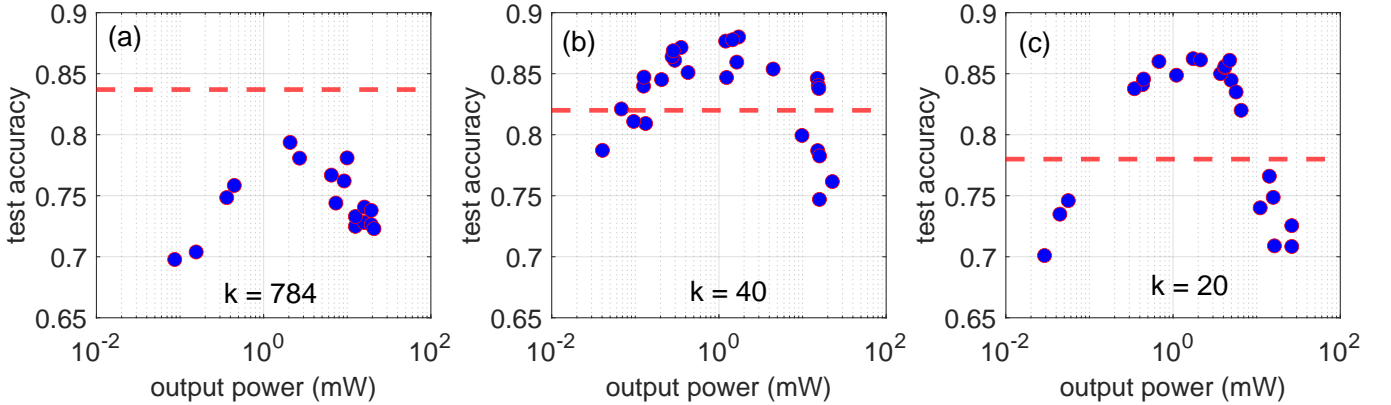


FIG. 7. Test accuracy as a function of input power for different encoding dimensions: (a) 784 PCs, (b) 40 PCs, and (c) 20 PCs. The red dashed line represents the linear baseline accuracy, achieved without the nonlinear fiber effects. Higher encoding dimensions (784 PCs) show limited improvement in accuracy, while intermediate dimensions (40 PCs) exceed the baseline at most power levels. Lower dimensions (20 PCs) exhibit sensitivity to power, with peak performance within a specific power range.

ments are observed, indicating a saturation effect where higher power fails to enhance performance. Panel (b) shows the results for encoding with  $d = k = 40$ . What is noteworthy is that here the system performs significantly better than when using the fully dimensional input with  $d = k = 784$ . Importantly, across most input power levels the test accuracy exceeds the linear baseline of 0.82, peaking at 0.880 at  $P_{\text{in}} = 1.72$  mW. However, at higher power levels, the accuracy drops to  $\sim 0.75$ , suggesting that excessive power introduces non-ideal interactions in the HNLF. Panel (c) shows the results for  $d = k = 20$ , where the system obtains a striking result, achieving nearly 10 % higher accuracy than the linear baseline. The performance is optimal within a specific power range of  $P_{\text{in}} = 0.4 \dots 1.4$  mW, and again accuracy decreases sharply outside this range. Best performances at the lowest  $P_{\text{in}}$  for similar performance are summarized in Tabel I.

These results provide very relevant insights for using NLSE substrates for physically implementing ELMs, here

in the context of an HNLF. Two effects have to be considered with regard to the best performances obtained. First, as shown in Fig. 2, for  $d > 50$  the optical ELM suffers from excessive injection losses, which is detrimental to the ELM dimensionality expansion. Second and more important are the considerations of input dimensionality  $d$  and ELM dimensionality  $\text{PCA}^{95}$  in the context of Cover’s theorem. Generally, our ELM’s dimensionality is limited to around  $\text{PCA}^{95} = 70$  for all tested configurations. This means by fundamental properties of random dimensionality expansion that the optical ELM can aid computation only if  $\text{PCA}^{95} > d$ . For  $\text{PCA}^{95} \leq d$  the optical system acts as a random dimensionality “reducer”, not an expander. Consequence to Cover’s theorem, classification under such conditions becomes harder using random projections. These are necessary, not sufficient criteria.

Finally, the drop in performance for powers exceeding a certain threshold is related to our consistency measurements in Section III A. Beyond this point, responses of

the network become inconsistent<sup>20</sup> for repeated injections of identical input information. As such, the system’s dimensionality potentially grows which in principle helps the approximation property, yet the system loses its approximation property and repeated injections of the same input will lead to different results. Table I summarizes the best performance results for the MNIST dataset.

TABLE I. Performance comparison between linear and nonlinear systems for different encoding configurations.

System	784 Channels	20 PC	40 PC
<b>Linear (benchmark)</b>	83.7%	78%	82%
<b>Nonlinear (experiment)</b>	75.5%	86%	88%
<b>Minimum output power</b>	$\sim 2$ mW	$\sim 0.5$ mW	$\sim 0.7$ mW

### Comparison Between HNFL and SMF

To further investigate the impact of fiber properties on system performance, a comparison was conducted between the HNFL and a standard SMF28 under the same range of input powers, results are presented in Fig. 8. With a mode field diameter typically twice that of the HNFL, the SMF28 exhibits a higher nonlinearity threshold characterized by nonlinear length  $L_{NL}$  after which nonlinear effects appear. Importantly,  $L_{NL} = \frac{1}{\gamma P_0}$ , where  $\gamma$  is the nonlinear coefficient of the fiber and  $P_0$  is the input peak power. In SMF28s, the larger core area reduces  $\gamma$ , either resulting in a longer  $L_{NL}$ , or one needs to compensate by increasing  $P_0$ . As shown in Fig. 8, the HNFL demonstrates superior performance at moderate input power levels due to its smaller core diameter and higher nonlinear coefficient  $\gamma$ . In contrast, the SMF28 requires significantly higher power to achieve comparable results due to its lower nonlinearity. This makes the HNFL a more energy-efficient option for nonlinear optical computing in scenarios where power constraints are critical. However, the SMF’s robustness at higher power levels as well as easier optical input coupling could be advantageous in applications requiring stability over long distances or higher power ranges.

## IV. DISCUSSION AND CONCLUSION

We demonstrated the feasibility of transforming nonlinear optical fibers into a versatile and efficient computational platform. Through detailed analysis, it was shown that key fiber parameters, such as dispersion and fiber length, play a pivotal role in defining the computational capacity of the system. Using PCA, the dimensionality of the system was evaluated, with results indicating that a range of 70 to 100 PCs can be achieved under optimal conditions for various fibers and input power levels. While higher dispersion tends to generate more PCs, potentially enhancing the computational

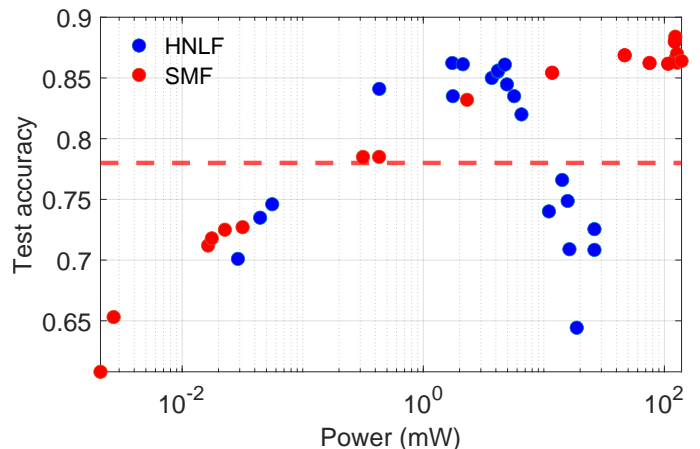


FIG. 8. Comparison of test accuracy for HNFL (blue) and SMF (red) as a function of input power. The HNFL, with a smaller core, exhibits nonlinear effects at lower power levels, while the SMF requires higher powers due to its larger core and longer nonlinear length. The red dashed line indicates the linear baseline accuracy.

capacity of the platform, it is important to consider the impact of other nonlinear effects. In the case of anomalous dispersion, the loss of spectral coherence can undermine repeatability, which we here characterize using the system’s consistency. Using the fundamental computing measures of dimensionality and consistency we provide a task-independent characterization and introduce these metrics to the ultrafast nonlinear optics community. They enable linking underlying nonlinear dynamical properties to computational capacity, paving the way for systematic analysis of computing via ultrafast NLSE and associated systems in experiments, numerical simulations, and numerically-assisted<sup>27</sup> as well as pure theoretical analysis.

The platform’s potential was further validated by successfully classifying the MNIST dataset with 10,000 examples, achieving accuracy levels that significantly exceeded those of a linear classifier and approaches 90% using only 40 input channels. These results underscore the ability of nonlinear optical fibers to exploit their intrinsic physical properties for advanced computational tasks, particularly by leveraging the interplay between nonlinearity, dispersion, and power.

Our optical computing system benefits from the ultrafast nature of light propagation, here leveraging linear as well as nonlinear propagation and mixing at such speeds and bandwidths. This ensures exceptional computational bandwidths and low latency. The input bandwidth is determined by the system’s input pulse width, which here amounts to  $\sim 1.8$  THz, which can be further expanded using shorter input pulses. Combined with the here demonstrated computing capability, one can imagine classifications of ultrafast phenomena on the input pulse’s timescales. When combined with spectral chirping, the processing of temporal aspects of data that are

dynamically evolving on these timescales becomes within reach. This provides prospects for an entirely new class of physical experiments as well as metrology in general.

In summary, this study highlights the significant potential of nonlinear optical fibers as computational platforms, offering a compelling combination of speed and computational capacity. Future work will require extensive mapping of the interplay between the different fiber parameters such as dispersion, input powers as well as the different classes of computational tasks. Here extensive numerical simulations will prove highly beneficial. Finally, replacing the OSA with a physical output layer and implementing in-situ learning<sup>5,6</sup> will implement a real-time computer with THz input data bandwidth, and inference rate given by the pulse repetition rate and essentially negligible latency on the nanosecond scale.

## V. FUNDING

The author acknowledge the support of the French Investissements d’Avenir Programme; Agence Nationale de la Recherche (ANR-15-IDEX-0003, ANR-17-EURE-0002, ANR-20-CE30-0004); the Academy of Finland (318082, 320165, 333949); and the European Research Council Consolidator Grant 101044777 (INSPIRE).

## VI. AUTHORCONTRIBUTIONS

The author confirms the sole responsibility for the conception of the study, presented result, and manuscript preparation. M.H. and P.R. constructed the Fourier-domain pulse shaper used in this work. M.H conducted all experiments. M.H., D.B., J. M. D. and G.G. planned the research project. All authors participated in interpreting the results and writing the manuscript.

## VII. CONFLICTOFINTEREST

Authors state no conflict of interest.

## VIII. DATAAVAILABILITYSTATEMENT

The datasets generated during the current study are available from the corresponding author on reasonable request.

## REFERENCES

- <sup>1</sup>B. J. Shastri, A. N. Tait, T. Ferreira de Lima, W. H. P. Pernice, H. Bhaskaran, C. D. Wright, and P. R. Prucnal, *Nature Photonics* **15**, 102–114 (2021).
- <sup>2</sup>J. Hall, J. Ye, S. Diddams, L.-S. Ma, S. Cundiff, and D. Jones, *IEEE Journal of Quantum Electronics* **37**, 1482–1492 (2001).
- <sup>3</sup>A. Momeni, B. Rahmani, B. Scellier, L. G. Wright, P. L. McMahon, C. C. Wanjura, Y. Li, A. Skalli, N. G. Berloff, T. Onodera, *et al.*, arXiv preprint arXiv:2406.03372 (2024).
- <sup>4</sup>L. G. Wright, T. Onodera, M. M. Stein, T. Wang, D. T. Schachter, Z. Hu, and P. L. McMahon, *Nature* **601**, 549 (2022).
- <sup>5</sup>X. Porte, A. Skalli, N. Haghghi, S. Reitzenstein, J. A. Lott, and D. Brunner, *Journal of Physics: Photonics* **3**, 024017 (2021).
- <sup>6</sup>A. Skalli, M. Goldmann, N. Haghghi, S. Reitzenstein, J. A. Lott, and D. Brunner, arXiv preprint arXiv:2409.01042 (2024).
- <sup>7</sup>M. Nakajima, K. Inoue, K. Tanaka, Y. Kuniyoshi, T. Hashimoto, and K. Nakajima, *Nature Communications* **13** (2022), 10.1038/s41467-022-35216-2.
- <sup>8</sup>G.-B. Huang, Q.-Y. Zhu, and C.-K. Siew, in *2004 IEEE international joint conference on neural networks (IEEE Cat. No. 04CH37541)*, Vol. 2 (Ieee, 2004) pp. 985–990.
- <sup>9</sup>S. Ortín, M. C. Soriano, L. Pesquera, D. Brunner, D. San-Martín, I. Fischer, C. Mirasso, and J. Gutiérrez, *Scientific reports* **5**, 14945 (2015).
- <sup>10</sup>M. Cucchi, S. Abreu, G. Ciccone, D. Brunner, and H. Kleemann, *Neuromorphic Computing and Engineering* **2**, 032002 (2022).
- <sup>11</sup>L. El Srouji, A. Krishnan, R. Ravichandran, Y. Lee, M. On, X. Xiao, and S. Ben Yoo, *APL Photonics* **7** (2022).
- <sup>12</sup>C. Wu, H. Yu, S. Lee, R. Peng, I. Takeuchi, and M. Li, *Nature communications* **12**, 96 (2021).
- <sup>13</sup>Y. Shen, N. C. Harris, S. Skirlo, M. Prabhu, T. Baehr-Jones, M. Hochberg, X. Sun, S. Zhao, H. Larochelle, D. Englund, *et al.*, *Nature photonics* **11**, 441 (2017).
- <sup>14</sup>B. Fischer, M. Chemnitz, Y. Zhu, N. Perron, P. Roztock, B. MacLellan, L. Di Lauro, A. Aadhi, C. Rimoldi, T. H. Falk, *et al.*, *Advanced Science* **10**, 2303835 (2023).
- <sup>15</sup>H. Jaeger and H. Haas, *science* **304**, 78 (2004).
- <sup>16</sup>A. Skalli, X. Porte, N. Haghghi, S. Reitzenstein, J. A. Lott, and D. Brunner, *Optical Materials Express* **12**, 2793 (2022).
- <sup>17</sup>M. Hary, L. Salmela, P. Ryczkowski, F. Gallazzi, J. M. Dudley, and G. Genty, *Optics Letters* **48**, 4512 (2023).
- <sup>18</sup>J. Dambre, D. Verstraeten, B. Schrauwen, and S. Massar, *Scientific reports* **2**, 514 (2012).
- <sup>19</sup>G. Marcucci, D. Pierangeli, and C. Conti, *Physical Review Letters* **125**, 093901 (2020).
- <sup>20</sup>A. Uchida, R. McAllister, and R. Roy, *Physical review letters* **93**, 244102 (2004).
- <sup>21</sup>T. Lyburn, T. Jüngling, and M. Small, in *International Conference on Artificial Neural Networks* (Springer, 2020) pp. 447–458.
- <sup>22</sup>B. A. Marquez, L. Larger, M. Jacquot, Y. K. Chembo, and D. Brunner, *Scientific Reports* **8**, 3319 (2018).
- <sup>23</sup>J. M. Dudley, G. Genty, and S. Coen, *Reviews of modern physics* **78**, 1135 (2006).
- <sup>24</sup>P. Y. Ma, A. N. Tait, T. F. De Lima, S. Abbaslou, B. J. Shastri, and P. R. Prucnal, *Optics express* **27**, 18329 (2019).
- <sup>25</sup>T. F. De Lima, A. N. Tait, M. A. Nahmias, B. J. Shastri, and P. R. Prucnal, *IEEE Photonics Journal* **8**, 1 (2016).
- <sup>26</sup>Y. LeCun, L. Bottou, Y. Bengio, and P. Haffner, *Proceedings of the IEEE* **86**, 2278 (1998).
- <sup>27</sup>A. V. Ermolaev, C. Finot, G. Genty, and J. M. Dudley, *Opt. Lett.* **49**, 4202 (2024).